Article

Characteristics and Geological Significance of Lacustrine Hydrothermal Sedimentary Rocks in the Yingejing Sag in Bayingebi Basin, Inner Mongolia, Northwestern China

Chaocheng Dai, Yu Zhang, Xirui Luo, Xiaodong Liu, Shumei Zhang, Jimei Zheng, and Long Xiang*

Read Online

ACCESS | Metrics & More | Article Recommendations

ABSTRACT: In order to promote site screening for high-level radioactive waste (HLW) disposal purposes, the characteristics of argillaceous rock (potential host rock) from the Yingejing Sag of the Bayingebi Basin, Northwest China have been well discussed. Results show that (1) Unlike argillaceous host rocks in foreign countries, the argillaceous rock mainly consists of analcite, dolomite, and albite; the contents of clay minerals are only about 10%. Five typical structures could be categorized, dominating by the massive structure. (2) Geochemical characteristics have the characteristics of abundance in deep source gas and liquid trace elements, a gentle right dip in the distribution pattern of rare-earth elements. (3) Petrological and geochemical characteristics determine the argillaceous rock as the genesis of lacustrine hydrothermal sedimentary rock. The hydrothermal sedimentary model also has been constructed, mainly controlled by tectonic activity of the Altyn Tagh fault from 100 to 120 Ma. The massive argillites with analcite and dolomite would lay the foundation for confirming the site for HLW disposal purposes in China.
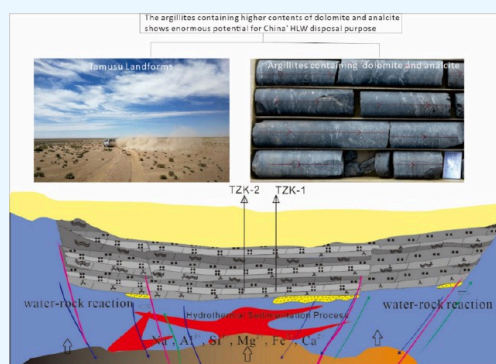
1. INTRODUCTION

Many nuclear countries have conducted detailed research on argillaceous rock as the host rock for high-level radioactive waste (HLW) repository as a result of minimal porosity, self-sealing ability, and almost no systematic exchange of materials with the environment. The Callovo−Oxfordian clay and the Opalinus clay have been systematically researched over 20 years as the host rock for HLW disposal repository in France and in Switzerland, respectively.[1−4] Currently, the Yingejing Sag (Tamusu area) in the Bayingebi Basin, Northwest China has been selected as a potential area for argillaceous rock repository purposes (Figure 1a). The target argillaceous rock formation is the lower Cretaceous Bayingebi formation with more than 500 m thickness, and the upper Bayingebi formation (K_1b^2) is the target formation. However, preliminary research found that the mineral compositions and typical structures are distinct from the typical argillaceous rock overseas, which has been defined as argillaceous rock containing analcite and dolomite. The argillaceous rock containing analcite and dolomite (target formation) cannot be explained through normal lacustrine sedimentation. Meanwhile, elementary issues such as the mineral assemblage and genesis are still pending, which have delayed the site-screening process.

Existing research studies near the Bayingebi Basin such as the Jiuxi Basin,[5] Santanghu Basin,[6] and Erlian Basin,[7] as well as continental lake basins such as the Junggar Basin[8] and the Hari Sag in the Yine Basin[9] (Figure 1b), pointed out that the lacustrine hydrothermal sedimentation may be the genesis of typical mineral compositions and structures.[10] It could be inferred that lacustrine hydrothermal sedimentation provides a path to address characteristics and the genesis of argillaceous rock containing analcite and dolomite. It is known that hydrothermal sedimentation is generally defined as the deposition that occurs when a hot water system circulating in marine or lacustrine basement rocks emerges near the interface.[11] During the hydrothermal sedimentation process, some typical structures are formed such as lamunar, speckled, and contemporaneous deformations. Meanwhile, their mineral compositions and elemental geochemical characteristics are different from those of the normal sedimentary rock. Therefore, focused on argillaceous rock containing analcite and dolomite (target formation), this study tries to find out (1) the petrological characteristics and mineralogical characteristics, (2) the elemental geochemical characteristics, and (3) the sedimentary patterns and control factors. This study is helpful in promoting the confirmation of site screening for HLW disposal purposes in China.
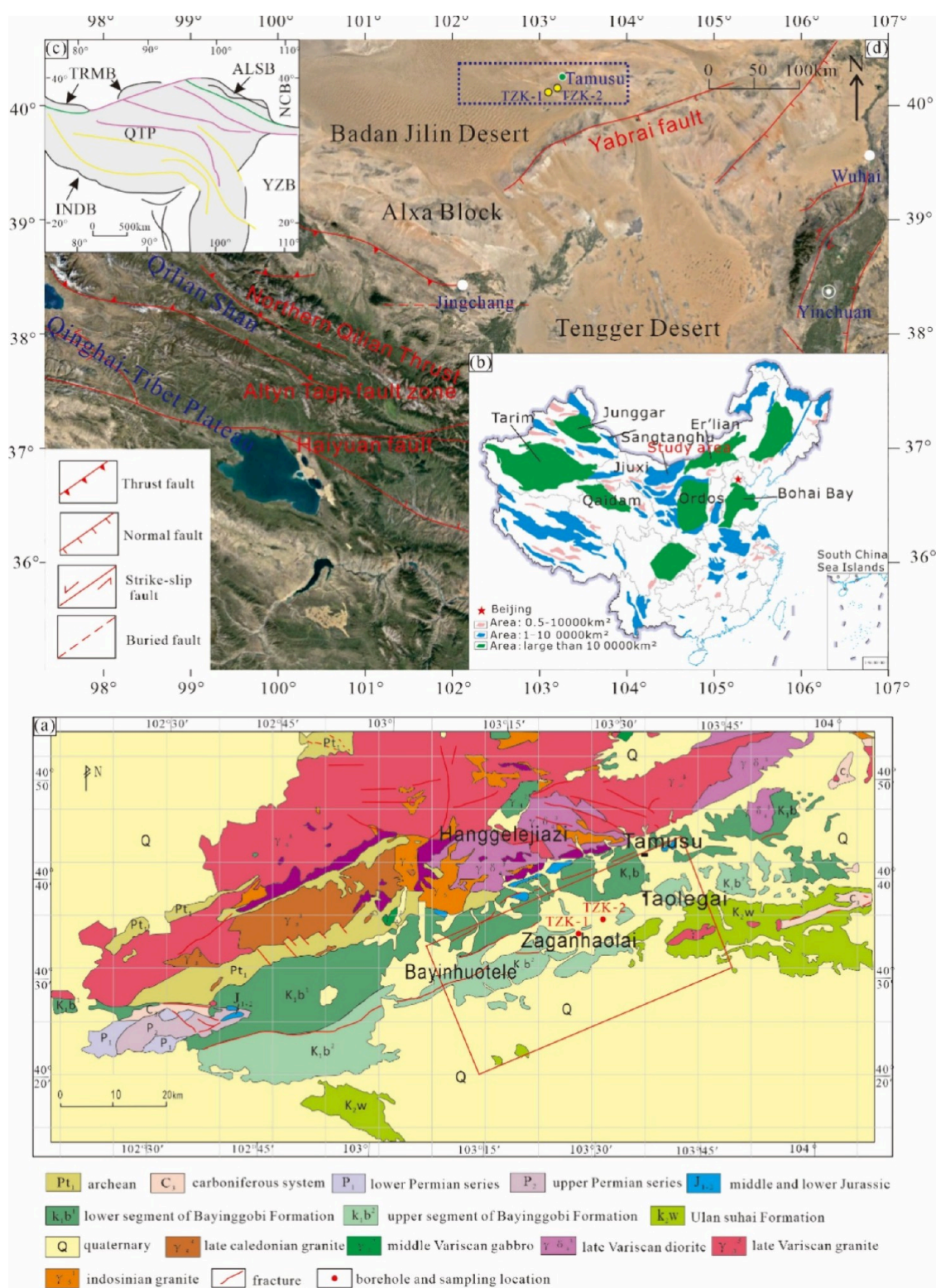
Figure 1. Regional geological map in the Yingejing Sag of Bayingebi Basin and ATF. Adapted with permission from ref 12 and 13. (a) Regional geological map of Yingejing Sag in the Bayingebi Basin. (b) Existing research areas of lacustrine hydrothermal sedimentation. (c, d) Tectonic setting of ATF. The blue dashed box of panel (d) denotes the location of panel (a). Copyright 2020 Elsevier. Copyright 2023 American Geophysical Union.

1.1. Geological setting. The Altyn Tagh fault (ATF) is a major, active intracontinental strike-slip fault system that separates the northern Tibetan Plateau from the Tarim block (Figure 1cd,[13,15]). The fault extends from the western Kunlun to the northeast side of the Qilian Shan with a total length greater than 2,000 km.[13,14] East of the northeastern most surface trace of

the ATF at approximately 97°15′E longitude, an array of faults that have a regional horsetail splay geometry in the southern Alxa block may kinematically link to the ATF and constitute an eastward extension of the fault system.[9] The ATF has been extending northeastward into the Mongolian region and is mainly characterized by a strike slip.[16,17] The Bayingebi Basin is
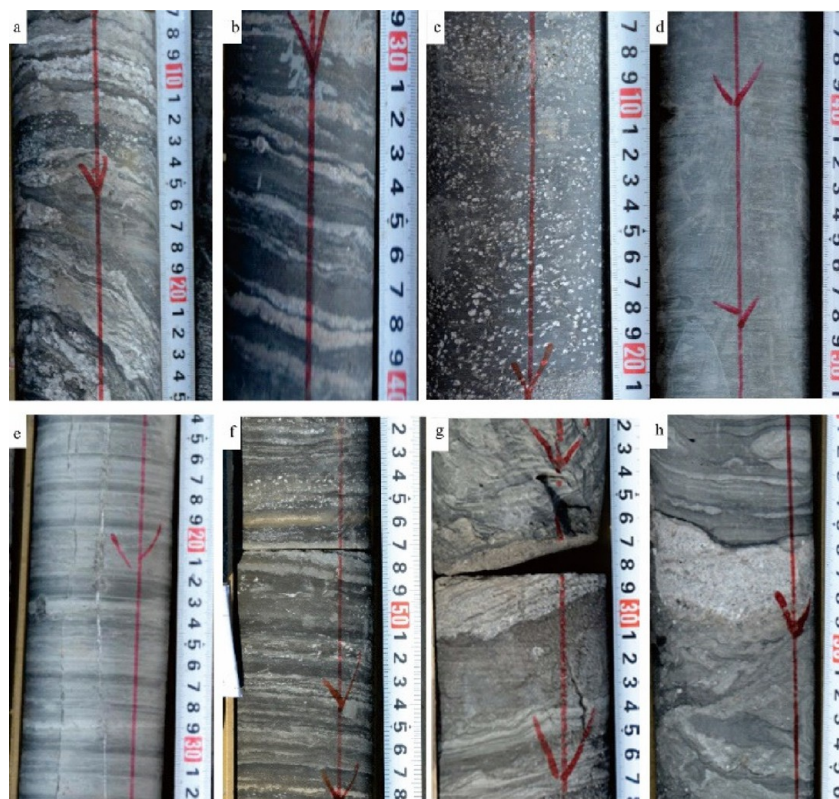
Figure 2. Characteristics of sedimentary structures in Bayingebi Formation argillites: (a) reticular argillite, TZK-2 well, 789.64 m; (b) vein argillite, TZK-2 well, 787.74 m; (c) speckled argillite, TZK-2 well, 565.81 m; (d) massive argillite, TZK-2 well, 325.00 m; (e) laminar argillite, TZK-2 well, 291.1 m; (f) laminar argillite, TZK-1 well, 675.70 m; (g) syngenetic deformation, TZK-1 well, 516.08 m; (h) tearing mud and gravel, TZK-1 well, 456.1 m.

located in the Southern Alxa block. The tectonic setting of the basin is the junction of the Tarim, Kazakhstan, Siberian, and North China plates. The basin spans four different geotectonic units[18,19] and is oriented in a near-EW direction. The Yingejing Sag is located at the southern end of the Bayingebi Basin and is oriented in a roughly NE direction, covering an area of approximately 9000 km² (Figure 1a). The sag has stable sedimentation, a small phase transition, and large depth variation, with deep burial in the south, slightly less burial in the north, and a simple basement structure. The overall trend of faults, the secondary faults of ATF, in the area is NE or near-EW. The near-EW direction represents earlier faults than the NE direction.[20] These faults control the interfacial structure of the basin as well as the type and spatial distribution of the sedimentary system.
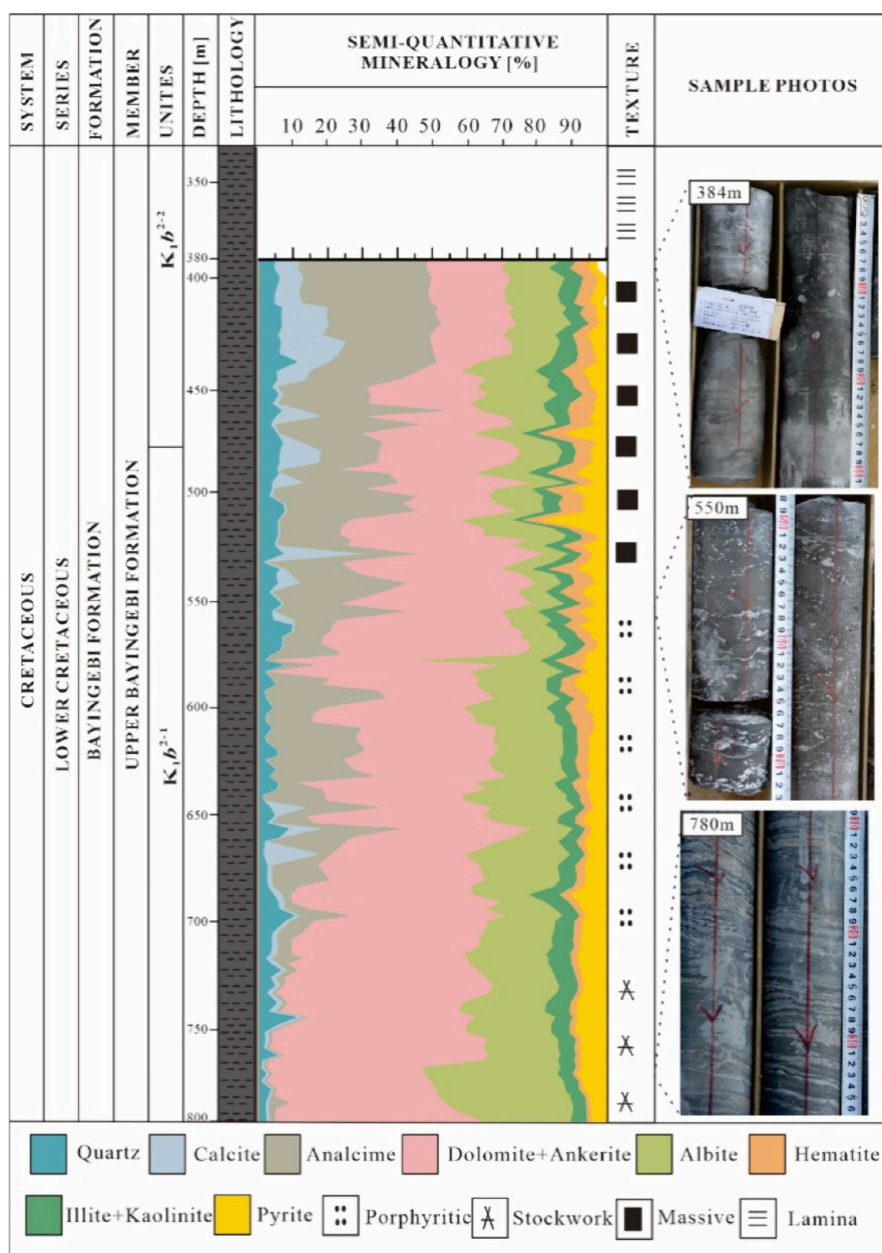
The basement of the Yingejing Sag is composed of Archean, Proterozoic, and Paleozoic metamorphic rocks. The caprock is mainly developed in the Jurassic, Cretaceous, and Quaternary strata. The Jurassic sedimentary strata are mainly composed of coal-bearing, coarse, and clastic rocks. The lithology is dominated by variegated conglomerate, sandstone, and fine sandstone; conglomerate and argillites are developed at the bottom, with dark gray and black tuff containing volcanic breccia at the top. Cretaceous strata comprise the sedimentary body of the caprock with a sediment thickness of more than 2200 m. The Lower Cretaceous sediments form the upper and lower portions of the Bayingebi Formation, namely, the K_1b^1 and K_1b^2. The main lithology of the lower portion of the Bayingebi Formation (K_1b^1) is composed of a purplish-red conglomerate and sandstone, occasionally mixed with siltstone and mudstone.

The upper portion of the Bayingebi Formation (K_1b^2) is composed of mainly gray-green and dark gray argillites and forms the target layer for the site of an HLW repository.

1.2. Petrological Characteristics of Argillites. Core observations and thin-section identification indicate that the upper portion of the Bayingebi Formation (target formation) contains reticular, speckled, massive, laminar, and contemporaneous deformations and shows an obvious regularity in the longitudinal direction. The lower portion is mainly composed of net veins, the middle and lower portions are speckled, the middle portion is homogeneously blocky, the middle and upper portions are mainly layered, and a number of gypsum layers are developed in the upper portion. A single layer of gypsum is generally 5−10 cm thick. Detailed analysis of the argillite structure was conducted by using a full core of the TZK-2 borehole.

1.2.1. Reticular Dolomite. The reticular structure is mainly developed at a depth of 730−800 m in the well, and the main vein-filling minerals are dolomite, ferric dolomite, analcite, and pyrite. The fractures range from wide to narrow, with reticular or irregular shapes (Figure 2a,b). Most of them are high-angle fractures interlaced with horizontal fractures. In the core, the width of the fracture in the filling veins is generally 0.5 mm−4 mm.

1.2.2. Speckled Analcite Dolomite. Speckled structures are mainly developed in the well at a depth of 550−730 m, and the particle composition of these speckled structures includes coarse-grained dolomite, calcite, pyrite, and analcite; the particle size is generally 2−6 mm. The core sample shows that these "snowflakes" are distributed within the matrix material (Figure

Figure 3. Lithology and mineralogy of the TZK-2 borehole in the Yingejing Sag.

2c), which is composed of mainly argillaceous dolomite or argillaceous sediments and is rich in organic matter; horizontal and small deformation beddings are locally developed.

1.2.3. Massive Dolomitic Analcite. The 260−550 m section of the well exhibits a massive structure, with massive argillite forming the main rock type in the upper portion of the Bayingebi Formation. The rocks are mainly gray to dark gray argillites with a small amount of grayish-white silty argillites (Figure 2d). The massive argillite has excellent uniformity, a high degree of consolidation, and a slippery feel; the cut surface is smooth and exhibits a conchoidal fracture. Under a polarized light microscope, the texture of the massive argillite is uniform and is usually associated with dolomite, calcite, a small amount of organic matter, and pyrite. The argillite is situated in the middle of the upper portion of the Bayingebi Formation, which is the main target stratum for the site of an HLW repository.

1.2.4. Laminar Dolomitic Analcite. The laminar structures are mainly developed at 31−260 m in the well, although they were also intermittently observed in other layers (Figure 2e,f). This is the most common sedimentary structure in the argillites of the TZK-2 well, and the white laminar structures are composed of various mineral combinations with thicknesses of several micrometers to several millimeters. Depending on the different types of minerals in the stratum, the common mineral combinations are as follows: (1) single dolomite layer, (2) dolomite analcite combination layer, and (3) dolomite and organic layer. When the thickness of the upper layer is increased to a few millimeters or even centimeters, it is termed a banded structure. In the banded structures, crystals are more euhedral and generally larger than those in the laminar structures.

1.2.5. Syngenetic Deformed Dolomitic Analcite. This structure is characterized by soft deformation and irregular crumpled bedding to form laminations or strips. The scale of
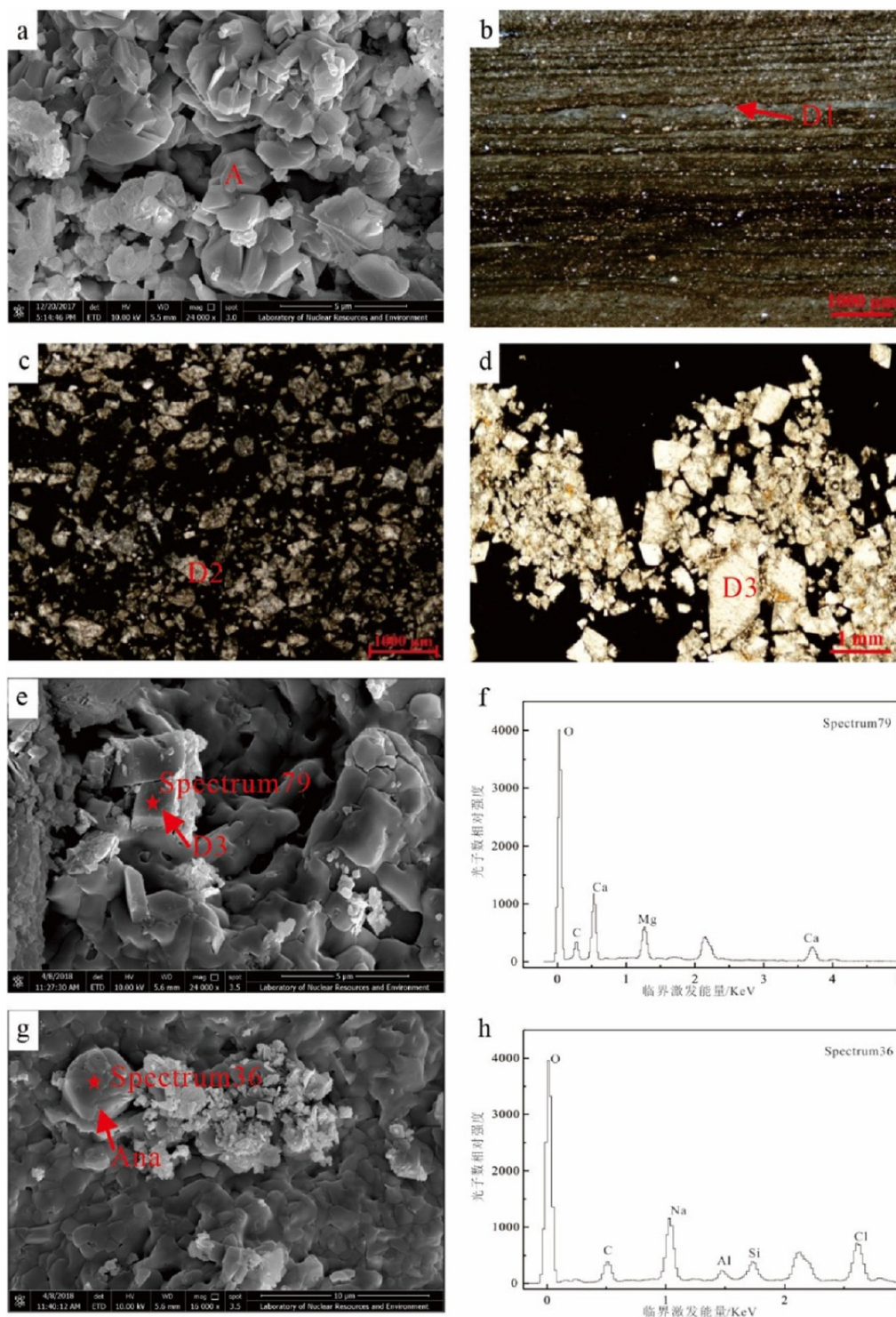
Figure 4. Typical mineral characteristics of the Bayingebi Formation argillites. (a) Typical tetrahedron of analcite, TZK-2 well, 413 m; (b) micritic dolomite and clay minerals form binary lamina, TZK-2 well, 313.25 m (single polarized light); (c) fine dolomite crystals are rhombic, TZK-1 well, 614 m, single polarized light; (d) coarse-grained dolomite crystals are rhombic, TZK-1 well, 595 m, single polarized light; (e) cubic mud microcrystalline dolomite particles, TZK-2well, 753.25m, SEM; (f) spectrum confirmation of panel (e); (g) analcite crystals are corroded into irregular tetragonal triaoctahedra, TZK-1 well, 593.53 m, SEM; (h) spectrum confirmation of (g). A, analcite; D1, micritic dolomite; D2, fine dolomite; D3, coarse dolomite.

deformation is generally several centimeters (Figure 2g). This type of deformation structure may be caused by unconsolidated or weakly consolidated laminations of a white mineral being locally disturbed by mud and gravel (Figure 2h).

2. SAMPLING AND ANALYSIS METHODS

All of the collected boreholes from the Yingejing Sag were carried out with water by single-core barreling techniques. The research samples were taken from the target formation (K_1b^2) were vacuum-sealed to maintain freshness. Based on the detailed

Table 1. Analysis Results and Characteristic Parameters of Geochemical Elements of Argillites in the Upper Bayingebi Formation[a]

no.	T41	T44	T52	T55	T58	T59	T60	T61	T66	T70
Al_2O_3	14.48	13.18	10.66	11.01	14.80	18.84	8.03	14.42	15.83	16.75
CaO	8.70	10.45	14.80	13.60	7.56	3.38	18.40	8.27	5.13	5.19
K_2O	2.66	2.72	2.27	2.49	2.23	2.94	2.08	2.28	2.97	2.74
Na_2O	4.71	4.18	3.37	3.49	5.63	7.16	2.54	5.40	5.92	6.77
P_2O_5	0.14	0.21	0.13	0.50	0.11	0.16	0.63	0.09	0.09	0.10
SiO_2	40.44	39.09	32.58	33.97	40.19	49.62	27.17	38.75	44.63	44.18
Ba	375	337	325	188	276	458	159	282.0	269	265.0
Sr	650	949	1155	1330	539	679	1720	739	595	526
Ni	33.40	26.40	22.60	26.60	27.80	37.50	18.70	24.50	27.00	19.20
V	134	176	158	201	153	159	139	156	141	131
Th	13.60	19.10	12.00	14.45	10.85	15.00	9.73	10.40	7.87	8.03
U	223.0	24.10	16.0	85.1	8.40	5.4	73.30	6.8	5.70	5.9
Rb	122.0	129.5	103.0	122.0	119.5	171.0	98.3	122.5	145.0	136.5
Sc	13.80	13.10	11.90	10.80	15.40	12.60	9.30	15.20	12.20	11.40
Zr	80	81	61	62	62	90	53	63	72	70
Co	19.7	17.6	14.4	14.2	18.5	20.9	11.7	15.7	18.0	12.6
Cu	45.9	43.1	34.4	36.3	42.4	55.6	27.6	41.4	44.0	36.9
La	34.8	38.2	31.8	29.5	37.9	45.8	19.0	42.3	44.5	31.2
Ce	72.7	76.1	65.7	56.6	76.0	87.6	37.0	84.6	88.6	63.4
Pr	7.14	7.83	6.60	5.90	7.88	9.22	3.98	8.57	8.84	6.71
Nd	25.9	28.0	23.8	21.7	28.3	32.9	14.2	30.8	30.6	24.5
Sm	4.85	5.06	4.32	4.09	5.22	6.15	2.65	5.60	5.36	4.59
Eu	0.93	0.93	0.87	0.77	1.04	1.10	0.54	1.05	1.00	0.92
Gd	4.14	4.04	3.76	3.61	4.56	4.78	2.31	4.84	4.46	3.77
Tb	0.61	0.62	0.54	0.57	0.64	0.68	0.32	0.67	0.61	0.55
Dy	3.60	3.44	3.16	3.29	3.62	3.89	2.12	3.84	3.30	3.00
Ho	0.70	0.72	0.61	0.73	0.68	0.73	0.44	0.73	0.63	0.61
Er	1.87	2.13	1.79	2.13	1.77	1.99	1.42	1.89	1.75	1.62
Tm	0.26	0.30	0.23	0.32	0.26	0.28	0.23	0.27	0.24	0.22
Yb	1.66	1.88	1.44	2.24	1.62	1.69	1.83	1.60	1.42	1.50
Lu	0.27	0.28	0.23	0.35	0.23	0.26	0.32	0.25	0.21	0.23
SiO_2/Al_2O_3	2.79	2.97	3.06	3.09	2.72	2.63	3.38	2.69	2.82	2.64
K_2O/Na_2O	0.56	0.65	0.67	0.71	0.40	0.41	0.82	0.42	0.50	0.40
CaO*	4.71	4.18	3.37	3.49	5.63	2.85	2.54	5.40	4.83	4.86
CIA	54.52	54.33	54.19	53.76	52.32	59.27	52.86	52.44	53.57	53.83
Co/Th	1.45	0.92	1.20	0.98	1.71	1.39	1.20	1.51	2.29	1.57
La/Sc	2.52	2.92	2.67	2.73	2.46	3.63	2.04	2.78	3.65	2.74
La/Yb	20.96	20.32	22.08	13.17	23.40	27.10	10.38	26.44	31.34	20.80
$\sum$REE	159.43	169.53	144.85	131.80	169.72	197.07	86.36	187.01	191.52	142.82
Sr/Ba	1.73	2.82	3.55	7.09	1.95	1.48	10.82	2.62	2.21	1.98
Sr/Cu	14.16	22.02	33.58	36.64	12.71	12.21	62.32	17.85	13.52	14.25
Rb/Sr	0.19	0.14	0.09	0.09	0.22	0.25	0.06	0.17	0.24	0.26
V/Ni	4.01	6.67	6.99	7.56	5.50	4.24	7.43	6.37	5.22	6.82
V/Ni + V	0.80	0.87	0.87	0.88	0.85	0.81	0.88	0.86	0.84	0.87
Ce_{anom}	0.0041	−0.0062	−0.0269	−0.0576	−0.0129	−0.0100	−0.1001	0.0087	0.0187	0.0037
δEu	0.62	0.61	0.65	0.60	0.64	0.60	0.65	0.60	0.61	0.66
δCe	1.05	1.01	1.04	0.98	1.01	0.97	0.98	1.01	1.02	1.01
LREE/HREE	11.16	11.64	11.32	8.95	11.68	12.78	8.61	12.27	14.18	11.42
Dy_N/Sm_N	0.45	0.41	0.44	0.49	0.42	0.38	0.48	0.42	0.37	0.40
no.	T79	T83	T85	T86	T99	T101	T102	T109	T115	T116
Al_2O_3	11.26	12.80	16.42	6.60	14.87	10.40	10.88	9.56	10.07	6.10
CaO	11.45	11.00	5.33	19.25	6.48	13.85	13.35	13.20	14.60	18.20
K_2O	1.78	1.82	2.53	1.65	2.19	1.53	2.54	1.87	1.73	1.53
Na_2O	4.87	5.60	6.80	2.49	6.54	4.78	3.98	4.21	4.58	2.58
P_2O_5	0.07	0.05	0.08	0.13	0.04	0.02	0.11	0.04	0.09	0.11
SiO_2	31.10	35.00	45.05	23.72	42.29	30.65	31.70	30.95	31.61	21.93
Ba	160	211.0	253.0	117	166	228	156	527.0	192	272
Sr	698	714	417	1340	474	1140	1320	2740	920	2270
Ni	27.30	9.60	25.90	15.40	22.10	8.40	19.50	20.00	18.80	18.90

Table 1. continued

no.	T79	T83	T85	T86	T99	T101	T102	T109	T115	T116
V	125	166	134	131	77	116	107	123	118	102
Th	10.60	5.78	7.15	18.40	10.85	3.09	12.10	5.91	12.00	13.70
U	10.50	3.68	4.85	26.00	2.94	3.80	14.30	14.65	18.00	28.9
Rb	71.9	80.7	137.0	53.7	71.5	56.8	116.0	66.3	57.6	47.2
Sc	14.10	18.20	10.50	9.20	9.80	11.60	12.30	8.50	10.00	8.20
Zr	55	56	78	46	57	45	44	41	54	39
Co	14.9	11.1	18.8	8.6	13.7	9.7	13.6	10.6	12.4	9.9
Cu	37.2	39.0	42.5	23.7	27.9	26.2	28.7	28.9	37.4	29.3
La	31.9	34.3	48.7	19.6	69.9	26.1	29.4	53.2	24.0	21.5
Ce	69.0	70.6	91.5	41.4	135.3	51.4	58.2	88.5	52.2	45.4
Pr	7.28	6.98	8.92	4.64	14.00	5.56	6.11	8.49	5.95	5.07
Nd	28.6	26.1	30.1	17.7	47.9	18.6	22.3	24.1	22.1	18.2
Sm	5.21	5.84	5.41	3.74	6.85	3.24	4.49	3.43	4.64	3.67
Eu	1.06	1.11	0.88	0.67	1.01	0.55	0.79	0.56	0.86	0.73
Gd	4.72	5.26	3.83	3.35	3.75	2.41	3.95	2.35	4.00	3.00
Tb	0.68	0.70	0.46	0.48	0.43	0.38	0.58	0.33	0.57	0.46
Dy	4.00	3.80	2.41	2.86	2.01	1.96	3.24	2.11	3.13	2.70
Ho	0.73	0.72	0.44	0.57	0.39	0.39	0.59	0.39	0.62	0.57
Er	1.96	1.81	1.17	1.63	1.01	0.99	1.62	1.17	1.64	1.52
Tm	0.27	0.25	0.17	0.25	0.15	0.15	0.22	0.16	0.23	0.23
Yb	1.66	1.55	1.05	1.58	0.95	0.99	1.34	1.16	1.46	1.43
Lu	0.25	0.23	0.16	0.25	0.15	0.17	0.20	0.18	0.23	0.20
SiO_2/Al_2O_3	2.76	2.73	2.74	3.59	2.84	2.95	2.91	3.24	3.14	3.60
K_2O/Na_2O	0.37	0.33	0.37	0.66	0.33	0.32	0.64	0.44	0.38	0.59
CaO*	4.87	5.60	5.06	2.49	6.35	4.78	3.98	4.21	4.58	2.58
CIA	49.43	49.57	53.29	49.89	49.65	48.39	50.89	48.16	48.04	47.69
Co/Th	1.41	1.92	2.63	0.47	1.26	3.14	1.12	1.79	1.03	0.72
La/Sc	2.26	1.88	4.64	2.13	7.13	2.25	2.39	6.26	2.40	2.62
La/Yb	19.22	22.13	46.38	12.41	73.58	26.36	21.94	45.86	16.44	15.03
$\sum$REE	157.32	159.25	195.20	98.72	283.80	112.89	133.03	186.13	121.63	104.68
Sr/Ba	4.38	3.38	1.65	11.45	2.86	5.00	8.49	5.20	4.80	8.35
Sr/Cu	18.76	18.31	9.81	56.54	16.99	43.51	45.99	94.81	24.60	77.47
Rb/Sr	0.10	0.11	0.33	0.04	0.15	0.05	0.09	0.02	0.06	0.02
V/Ni	4.58	17.29	5.17	8.51	3.48	13.81	5.49	6.15	6.28	5.40
V/Ni + V	0.82	0.95	0.84	0.89	0.78	0.93	0.85	0.86	0.86	0.84
Ce_{anom}	0.0074	0.0005	−0.0005	−0.0953	0.0184	−0.0349	−0.0039	−0.0301	−0.0410	−0.0985
δEu	0.64	0.60	0.56	0.57	0.55	0.58	0.56	0.57	0.60	0.65
δCe	1.05	1.04	0.98	1.01	0.98	0.98	0.99	0.91	1.02	1.01
LREE/HREE	10.02	10.12	19.14	8.00	31.10	14.17	10.33	22.71	9.24	9.35
Dy_N/Sm_N	0.46	0.39	0.27	0.46	0.18	0.37	0.44	0.37	0.41	0.45
no.	T117	T123	T127	T128	T133	T134	T141	T146	T154	T156
Al_2O_3	5.72	11.59	9.91	10.68	8.04	8.89	7.06	8.41	8.69	6.77
CaO	19.55	10.80	12.55	10.60	15.88	14.45	16.90	13.90	12.55	15.75
K_2O	1.22	2.68	3.47	2.87	2.33	2.10	2.85	1.34	2.72	1.27
Na_2O	2.60	4.14	3.14	3.26	2.80	3.58	2.07	4.10	3.16	3.14
P_2O_5	0.02	0.02	0.02	0.04	0.29	0.11	0.05	0.02	0.09	0.04
SiO_2	18.80	33.65	32.27	36.31	26.06	28.20	22.86	29.34	28.66	24.65
Ba	83	228	706.0	224.0	101.0	156	152	165	223.0	172.5
Sr	1890	1180	1540	1090	1290	910	1730	1230	1180	1090
Ni	12.40	18.10	20.60	23.10	22.90	17.40	14.30	18.30	21.60	17.90
V	109	133	119	96	131	105	111	72	82	93
Th	3.22	4.73	8.60	3.46	18.60	16.85	3.67	2.24	5.86	3.36
U	13.90	11.30	9.5	27.60	73.90	27.00	16.65	6.34	12.10	7.0
Rb	35.6	119.0	132.5	137.0	70.9	63.3	81.0	56.8	45.3	52.8
Sc	10.20	10.70	8.60	7.30	9.60	10.10	8.80	6.80	6.00	7.80
Zr	24	51	43	62	42	41	53	42	40	37
Co	7.5	13.5	11.5	13.3	12.4	12.2	8.9	9.8	9.3	8.9
Cu	18.6	37.3	30.1	34.3	35.0	33.9	29.3	27.5	31.5	22.3
La	13.0	25.6	40.1	15.6	28.6	23.0	12.5	31.8	21.9	19.3
Ce	27.3	50.5	77.5	30.8	59.7	50.3	26.1	62.5	44.1	38.9

Table 1. continued

no.	T117	T123	T127	T128	T133	T134	T141	T146	T154	T156
Pr	2.67	5.30	7.85	3.17	6.57	5.70	2.79	6.60	4.55	3.79
Nd	9.2	18.1	25.4	10.8	23.5	21.0	9.9	22.3	17.1	13.3
Sm	1.61	3.71	4.37	2.06	4.29	4.28	1.89	3.46	3.14	2.21
Eu	0.28	0.72	0.77	0.43	0.97	0.84	0.36	0.68	0.61	0.42
Gd	1.48	3.14	3.10	1.65	4.03	3.69	1.65	2.75	2.54	1.70
Tb	0.23	0.44	0.48	0.27	0.59	0.53	0.24	0.34	0.36	0.25
Dy	1.30	2.51	2.58	1.73	3.37	2.99	1.47	2.03	2.03	1.41
Ho	0.28	0.48	0.51	0.35	0.63	0.58	0.32	0.43	0.39	0.29
Er	0.88	1.34	1.48	0.90	1.79	1.51	0.90	1.16	1.05	0.84
Tm	0.13	0.19	0.19	0.13	0.27	0.21	0.14	0.17	0.16	0.14
Yb	0.83	1.21	1.18	0.88	1.55	1.31	0.89	1.06	1.09	1.01
Lu	0.13	0.19	0.16	0.13	0.22	0.20	0.14	0.17	0.16	0.16
SiO_2/Al_2O_3	3.29	2.90	3.26	3.40	3.24	3.17	3.24	3.49	3.30	3.64
K_2O/Na_2O	0.47	0.65	1.11	0.88	0.83	0.59	1.38	0.33	0.86	0.40
CaO*	2.60	4.14	3.14	3.26	2.80	3.58	2.07	4.10	3.16	3.14
CIA	47.12	51.40	50.41	53.21	50.34	48.98	50.25	46.85	49.01	47.28
Co/Th	2.33	2.85	1.34	3.84	0.67	0.72	2.43	4.38	1.59	2.65
La/Sc	1.27	2.39	4.66	2.14	2.98	2.28	1.42	4.68	3.65	2.47
La/Yb	15.66	21.16	33.98	17.73	18.45	17.56	14.04	30.00	20.09	19.11
$\sum$REE	59.32	113.43	165.67	68.90	136.08	116.14	59.29	135.45	99.18	83.72
Sr/Ba	22.66	5.18	2.18	4.87	12.77	5.83	11.42	7.48	5.29	6.32
Sr/Cu	101.61	31.64	51.16	31.78	36.86	26.84	59.04	44.73	37.46	48.88
Rb/Sr	0.02	0.10	0.09	0.13	0.05	0.07	0.05	0.05	0.04	0.05
V/Ni	8.79	7.35	5.78	4.16	5.72	6.03	7.76	3.93	3.80	5.20
V/Ni + V	0.90	0.88	0.85	0.81	0.85	0.86	0.89	0.80	0.79	0.84
Ce_{anom}	−0.0444	−0.0866	−0.0029	−0.1386	0.0409	0.0370	−0.2022	−0.0884	−0.0326	−0.0538
δEu	0.55	0.63	0.61	0.69	0.70	0.63	0.61	0.65	0.64	0.64
δCe	1.06	0.99	0.99	1.00	1.01	1.03	1.02	0.99	1.01	1.03
LREE/HREE	10.28	10.94	16.11	10.41	9.93	9.54	9.31	15.70	11.75	13.43
Dy_N/Sm_N	0.49	0.41	0.36	0.51	0.48	0.42	0.47	0.36	0.39	0.39

[a]The unit for major elements is %, and the unit for trace and rare-earth elements is $\mu g/g$. LREE = La + Ce + Pr + Nd + Sm + Eu; HREE = Gd + Tb + Dy + Ho + Er + Tm + Yb + Lu; $\sum$REE = LREE + HREE; δEu = $Eu_N/(Sm \times Gd)_N^{1/2}$; δCe = $Ce_N/(La \times Pr)_N^{1/2}$. Standardized data adopt Taylor's standard value. CIA = $[Al_2O_3/(Al_2O_3 + CaO^* + Na_2O + K_2O)] \times 100$, where the unit of each principal component in the formula is the molar quantity, and CaO* refers to CaO in silicate minerals (excluding CaO in carbonate and phosphate minerals). Ce_{anom} = lg$[3Ce_U/(2La_U+Nd_U)]$ calculated based on the North American shale

observation and description of the argillite cores of the TZK-1 and TZK-2 wells, 150 thin sections were made to observe the microstructural characteristics of the argillite. Thirty samples were selected for analysis with scanning electron microscopy to further observe the crystal structure and micromorphological characteristics of the main minerals in the argillite. A total of 116 samples were selected for full-rock X-ray diffraction analysis to determine the main mineral species and the composition, in the vertical and horizontal directions, of the Bayingebi Formation argillites. In addition, 30 samples were tested for trace and rare-earth elements. All the samples were researched in an orderly manner according to the corresponding experimental standards. The samples were representative, and the data were informative and reliable. Scanning electron microscopy, X-ray diffraction analysis, and the electron probe microanalysis (EPMA) tests (JXA-8530F Plus, Japan) were conducted at the State Key Laboratory of Nuclear Resources and Environment of East China University of Technology. The analytical instruments included a Nova Nano SEM450 emission scanning electron microscope from FEI Czech Co., Ltd. (with X-Max20 energy), a spectrometer, and a German Bruker D8 ADVANCE polycrystalline X-ray diffractometer. The EPMA analytical conditions were as follows: an acceleration voltage of 15 kV, a current of 20 nA, and a beam spot diameter of <2 μm, with a 10 s counting time for the major elements and 20 or 40 s for the minor elements.

Analysis of trace and rare-earth elements was completed at Aussie Analytical Testing (Guangzhou) Co., Ltd. The experimental instruments included an inductively coupled plasma atomic emission spectrometer, produced by Agilent, USA, and an inductively coupled plasma mass spectrometer (model PerkinElmer Elan 9000, USA). The experiments were conducted with the system settings, accuracy, and precision of the detection method (relative deviation and relative error) controlled at <10 ± 5%.

3. ANALYSIS RESULTS

3.1. Mineralogical Characteristics of Argillites. The target mudstone formation is mainly composed of three mineral species (Figure 3): carbonates (dolomite and ankerite), albite, and analcite. In addition, small amounts of evenly distributed clay minerals (mainly illite and kaolinite), quartz, calcite, hematite, and pyrite are also present. Carbonate minerals are abundant in all samples. In particular, the mass fractions of dolomite and ankerite ranged from 3 to 50% and from 4 to 25%, respectively, with average mass fractions of 28 and 13%, respectively. The mass fractions of analcite and calcite ranged from 1 to 43% and from 0.2 to 23%, respectively, with averages of 17 and 3%, respectively. Both analcite and calcite decreased rapidly with depth. The total mass fractions of clay minerals are less than 10%, dominated by illite and kaolinite with average
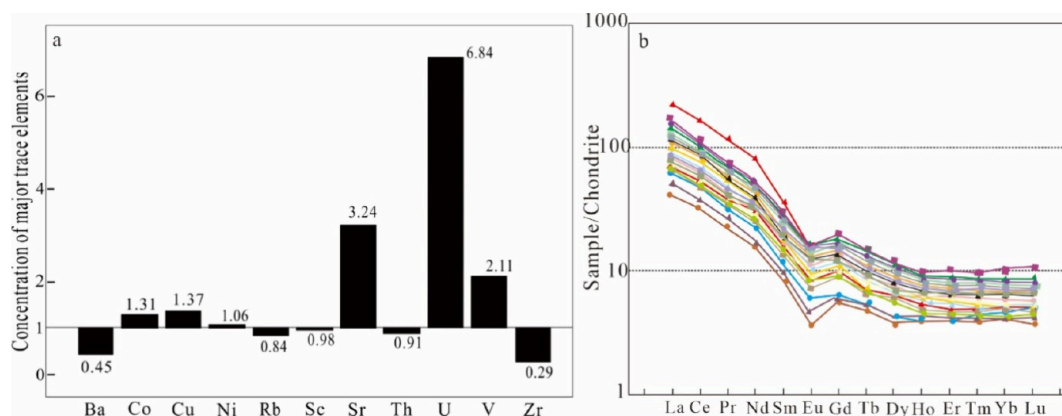
Figure 5. Characteristics of trace and rare earth elements: (a) concentration coefficients of trace elements and (b) rare-earth element distribution patterns.

mass fractions of 3 and 2%, respectively. The typical analcite and dolomite are described in detail.

3.1.1. Analcite. The ideal chemical formula for analcite is $NaAlSi_2O_6 \cdot H_2O$. It is colorless and transparent under a single polarizing microscope and has a low−low protrusion. Under orthogonal polarized light, analcite exhibited a first-order gray interference color with full or weak extinction. The crystals had a high degree of self-formation, which were self-shaped and semiself-shaped, and were easily distinguishable from the other surrounding minerals. The single crystal of analcite examined with a scanning electron microscope was a typical tetragonal octahedron (Figure 4a,g). Due to the unique ion-exchange performance of the analcite, it has a strong adsorption capacity for nuclides. Therefore, the existence of this type of analcite significantly improved the physical properties of the host rocks in the Bayingebi Formation.

3.1.2. Dolomite. Dolomite is the main rock-forming mineral of the argillites. Based on the crystal size, shape, and distribution, three types of dolomites were developed, namely, mud-crystal dolomite (Figure 4b,e), powdered crystal dolomite, and coarse-grained dolomite (Figure 4c,d). Dolomite is often distributed in strips within the argillite. Under a microscope, mud-crystal dolomites have a small particle size and are miscible with terrigenous clastic minerals to distinguish their crystal forms. Under scanning electron microscopy, the crystal size of the mud-crystal dolomite was uniform and the particle size was 2−10 μm, while the grain size of the powdered dolomite was generally 30−200 μm. Compared to the mud-crystal dolomite, the crystal of silty dolomite has a high degree of automorphism (semi-automorphic to automorphic), and the hole is relatively clean. Scanning electron microscopy revealed that rhombohedral dolomite often coexists with analcite with a high degree of self-formation. The coarse-grained dolomite is rhombohedral, and its grain size can reach 0.5 mm.

3.2. Geochemical Characteristics. *3.2.1. Major Element Features.* The oxide contents of the main minerals of the upper argillite in the Bayingebi Formation are listed in Table 1. The oxides are mainly SiO_2 (18.80−49.62%), CaO (3.38−19.6%), and Al_2O_3 (5.72−18.84%). The average values for these oxides were 33.18, 10.38, and 9.59%, respectively, while P_2O_5 (0.02−0.63%) had an average value of less than 1%.

3.2.2. Characteristics of Trace and Rare-Earth Elements. The average values of trace elements in the argillites of the Bayingebi Formation (Table 1) can be determined by dividing the average content of the upper continental crust (UCC)

elements to obtain the concentration coefficients of the corresponding elements (Figure 5a). The argillite is clearly enriched in Sr, U, and V. The set coefficient is >2, especially for U, which is abnormally enriched in the research area, to approximately 0.01−0.06%, reaching an industrial-grade requirement. The uranium deposit in this area has been explored based on the sandstone type. However, the discovery of several layers of industrial ore bodies in the argillites of the deep-lake facies is difficult to explain with the interlayer oxidation zone model, which has led to a lack of clarity around the metallogenic mechanism of uranium in this area. The proportions of Co, Cu, and Ni are close to the average value of the upper crust, displaying a slight enrichment. The proportion of Ba, Rb, Sc, Th, and Zr are lower than the average value of the upper crust, showing a relative loss. The Sr content in the sample (a large ion lithophile element) is much higher than the average value of the upper crust, up to 2740×10^{-6} (μg), while Zr and other elements are mainly present in the coarse minerals and are relatively depleted in the fine-grained argillites. Se and S have similar properties, and their content in the upper portion of the Bayingebi Formation is 1×10^{-6} (μg), which is higher than their abundance in the UCC (8.83×10^{-8} μg).[21] In combination, they form an independent selenium-containing mineral.

Rare-earth element concentrations vary widely in the argillites, with a total amount of 59.29 to 283.80 μg/g and an average of 139 μg/g, which is slightly lower than the UCC average (146.37 μg/g). The ratio of light-to-heavy rare-earth elements (LREE/HREE) varies from 8 to 31.10, with an average of 12.52. The argillites are enriched in LREEs and depleted in HREEs, and the distribution curve of LREEs has a steep slope (La−Eu segment), showing a distinct "right-dip" type. The sample δEu is approximately 0.545−0.703, with an average of 0.616, which is a moderately strong negative anomaly. The δCe values are approximately 0.908−1.059, with an average of 1.01. The average distribution pattern of rare-earth elements and UCC elements (Figure 5b) shows a consistent change characteristic.

4. DISCUSSION

4.1. Hydrothermal Sedimentation Process. During the process of spraying the bottom of a sea (or lake), hot water is filled and replaced in a hydrothermal channel below the spout, and the bottom of the sea (or lake) above the spout passes through the cold water. The substances carried in the hot water interact with the cold water and precipitate at the bottom of the
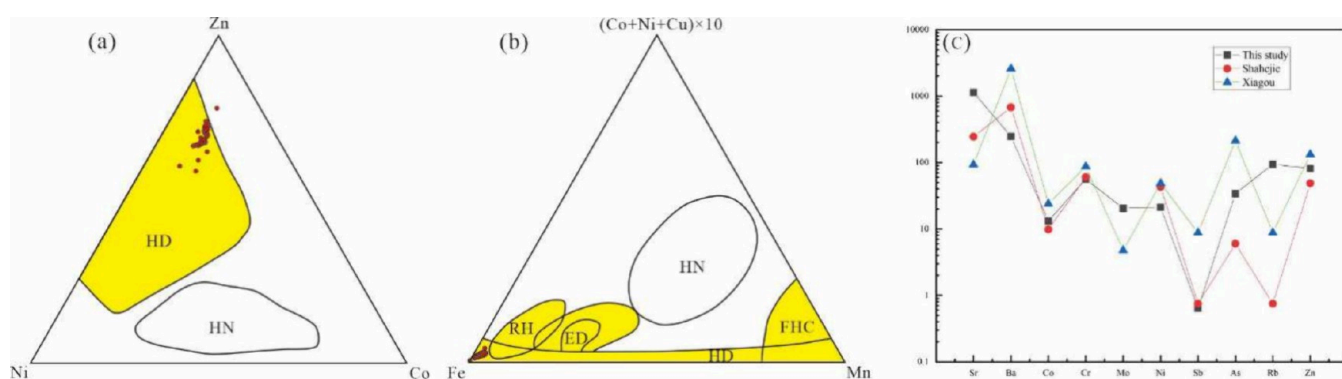
Figure 6. Element features for hydrothermal sediments: (a) Ni vs Co vs Zn ternary diagram and (b) Fe vs Mn vs (Cu+Co+Ni) × 10 ternary diagram. (c) Trace element comparisons from typical hydrothermal sedimentary areas; HD, hot water deposits; HN, water deposits; RH, red sea hydrothermal deposits; ED, Eastern Pacific hydrothermal deposits of metallic minerals; FHC, Franciscan hydrothermally deposited siliceous rocks.

Table 2. EPMA Analysis of Analcite and Dolomite in Hydrothermal-Sedimentary Rock[a]

| minerals	borehole	depth (m)	test points	K_2O	Al_2O_3	SiO_2	FeO	CaO	Na_2O	MgO	total
analcite	ZHK88-15	240	18-001-s1	0.035	21.321	61.479	0.084	0.225	9.014	0.131	92.295
			18-001-s2	0.044	21.802	60.209	0.115	0.249	6.424	0.088	88.931
			18-001-s3	0.069	21.138	57.698	0.037	0.113	12.986	0.031	92.072
			18-001-s4	0.072	20.257	59.085	0.089	0.271	11.938	0.045	91.767
			18-001-s5	0.193	20.224	60.065	0.672	0.067	10.877	0.162	92.306
			18-001-s6	0.013	20.383	57.487	0.052	0.218	12.265	0.03	90.467
	TZK-2	686	T124-s1	0.061	19.988	60.377	0.115	0.078	12.161	0.043	92.853
			T124-s2	0.329	20.741	61.255	0.182	0.469	8.592	0.244	91.812
			T124-s3	0.041	20.267	59.349	0.074	0.018	12.297	0.013	92.094
			T124-s4	0.238	19.87	59.339	0.165	0.433	11.918	0.265	92.234
			T124-s5	0.029	19.834	60.346	0.067	0.031	12.075	0.011	92.393
	ZKH104-8	224	18-016-s1	0.012	19.77	64.781	0.006	0.097	8.269	0.01	92.989
			18-016-s2	0.027	20.8	63.982	0.043	0.181	8.402	0.045	93.484
			18-016-s3	0.265	19.494	65.843	0.112	0.264	7.374	0.133	93.577
	TZK-2	493	18-018-s1	0.024	20.854	61.991	0.072	0.266	10.911	0.004	94.122
			18-018-s2	0.025	20.101	61.998	0.107	0.251	10.004	0.104	92.59
			18-018-s3	0.011	20.329	61.034	0.052	0.736	11.019	0.023	93.204
	TZK-1	523	523-s5	0.027	19.951	62.046	-	0.065	10.694	-	92.783
	TZK-2	538	18-021-s2	0.029	20.538	62.235	0.038	0.152	11.163	0.052	94.207
	TZK-2	523	18-019-s2	0.021	20.619	63.112	0.099	0.698	8.129	0.517	93.204
dolomite	TZK-1	593	593-s5	0.183	0.295	0.926	0.569	29.256	0.214	20.83	52.695
			523-s1	0.064	0.131	6.55	0.29	28.731	0.137	18.824	54.908
		523	523-s2	0.091	0.242	0.537	0.27	33.036	0.162	19.413	53.813
			523-s3	0.149	0.388	0.947	0.367	30.092	0.127	20.552	52.834
	TZK-2	715	T132s	0.198	0.259	0.959	0.186	29.273	0.263	21.15	52.429
		686	T124-s8	0.105	0.36	0.873	1.216	28.888	0.223	19.296	50.986
		538	18-021-s1	0.171	0.877	2.427	1.465	29.284	0.302	18.675	53.513

[a]Note: EPMA tests completed in ECUT by JXA-8230

sea (or lake), and two diagenetic or metallogenic systems are formed during this hydrothermal flow. Saddle-like and zebra-like structures have been proven to have a hydrothermal metasomatic genesis, associated with tectonic faults in marine hydrothermal dolomite.[9,22] In lake-phase hydrothermal sediments, layered structures and plaques are considered to be important features formed by lacustrine hydrothermal fluids, reflecting pulsating hydrothermal eruptions and zonal deposition.[5,7,8] From the bottom to the top of the upper portion of the Bayingebi Formation, the argillites exhibit a network of veins, a patchy structure, a massive structure, and a layered structure. The upper portion of the argillites has a large number of thin gypsum layers. The vertical structure of the argillites is very similar to that of hot water.

Based on the temperature characteristics and mineral colors, hydrothermal deposition is divided into a "white chimney" type and a "black chimney" type. The first type forms light-colored minerals, such as carbonates, silicates, and sulfates, at lower temperatures, and the second type forms mainly dark minerals, such as sulfides and oxides, at higher temperatures. Most lake-facies hydrothermal deposits discovered to date have been characterized as the "white chimney" type, and the main minerals formed are aluminosilicates (such as albite, analcite, and tourmaline), sulfates (such as barite) and carbonates (such as dolomite and siderite).[7] Analcite, dolomite, ferruginous dolomite, fluorite, galena, sphalerite, uranium minerals, and selenium minerals occur in the upper portion of the Cretaceous Bayingebi Formation in Yingejing Sag. To determine if the
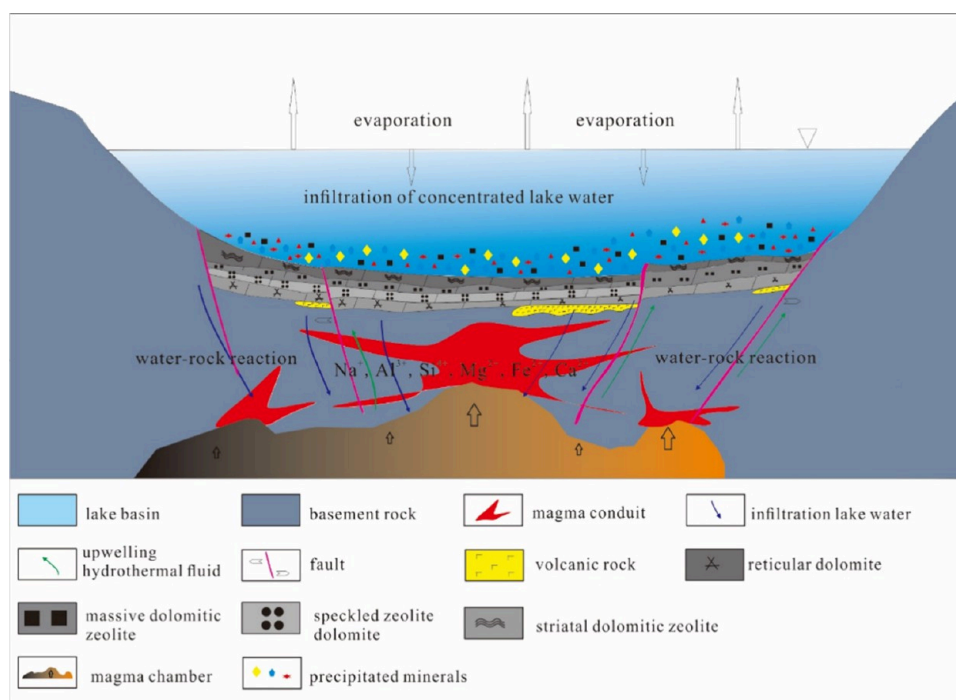
Figure 7. Sedimentary model of lacustrine hydrothermal rocks in the Yingejing Sag, Bayingebi Basin. Adapted with permission from ref 19. Copyright 2023 Springer.

analcite in the study area is a metamorphic or primary mineral, the authors examined samples with a microscope and found that some samples contain montmorillonite, with contents less than 5%; montmorillonite is a layered silicate. Medium-water minerals are easily dehydrated and converted to illite during low-grade metamorphism. No low-grade metamorphic minerals, such as turbidite and grapevine, were found in the samples analyzed. When the metamorphic temperature reached approximately 200 °C, the following reactions occurred in analcite and quartz:

$$Na_2[AlSi_2O_6]_2 \cdot 2H_2O + 2SiO_2 = 2Na[AlSi_3O_8] + 2H_2O$$
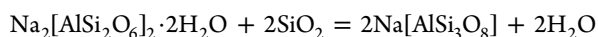
Albite was formed; however, in the mineral profile, the proportions of analcite, quartz, and albite did not have a reciprocal relationship. Under the microscope, there was no evidence of a reaction between analcite and quartz to form albite; hence, the mineral composition of the argillites cannot be explained by metamorphism. The formation of Na^--, Ca^--, and Mg^{2+}-rich minerals may be attributable to the alkaline hydrothermal fluids rich in Na^+, Ca^{2+}, and CO_3^{2-} gushing out of the lake bottom, mixing with the lake water, and directly crystallizing or forming hydrothermal sedimentary minerals in the early stage of metasomatism. This indicates that there may have been long-term white chimney-type hydrothermal activity in the Early Cretaceous, and the hydrothermal fluids had different properties during different periods. Different types of hydrothermal fluids mixed with cold lake water to form different types of minerals.

The geochemical characteristics of hydrothermal sedimentary rocks are quite different from those of normal sedimentary rocks. Geochemical analysis can be used to effectively distinguish the sediment types. Iron−manganese oxide is often used as an important indicator of hydrothermal deposition.[11,23] For instance, high Fe and Mg contents are considered typical of hydrothermally formed dolomite.[24] The main minerals of the argillite samples in the upper portion of the Bayingebi Formation showed obvious Fe and Mg enrichment. The average proportions of TFe_2O_3 and MnO were 5.47 and 0.11%, which were higher than the corresponding average contents of the UCC (4.93 and 0.07%, respectively).[25] U and Se elements were abnormally enriched, with U as high as 0.01−0.06% locally and Se contents of 1×10^{-6} (μg), 8.83×10^{-8} times higher than its abundance in the crust.[21] Se and S have similar properties and are much more enriched in hydrothermal fluids than in lake water. Ternary diagrams of Fe vs Mn vs (Cu + Co + Ni) × $10^{11,26}$ (Figure 6a) and Ni vs Co vs Zn (Figure 6b)[27] are widely used for the discrimination of hydrothermal sediments. On the ternary diagram, all argillite samples in the study area are plotted within the hydrothermal deposition zone, indicating long-term hydrothermal activity during the Early Cretaceous sedimentation of the Yingejing Sag. The collected trace element data from a typical hydrothermal sedimentary area such as Shahejie Formation and Xiagou Formation show a consistent trend of change, contributing to the genesis of hydrothermal sedimentary (Figure 6c).

The Si/Al ratios of analcite are characterized by high silica (2.316−2.866, avg. 2.545) (Table 2), which is obviously higher than the sedimentary diagenetic type of analcite formed by sedimentary diagenesis and low-grade metamorphism and higher than that of low silicon analcite that is directly crystallized from highly alkaline water. This type has Si/Al ratios that are closer to those of high silicon analcite, which is commonly affected by siliceous volcanic glass and alkaline hydrothermal solution.[12] Therefore, analcite may have formed by the direct crystallization of alkaline hydrothermal fluids.

4.2. Tectonic Setting of Hydrothermal Sedimentary Rocks. The Bayingebi Basin entered a stage of intraplate structural tectonic influence during the Mesozoic period and, during the Triassic−Jurassic period, developed a "rift and pull" sub-basin.[28] In the Early Cretaceous, the basin was an

extensional tectonic setting and a large number of normal faults developed at the edge of the basin, which caused the Yingejing Sag to form a double-breaking ground-type lake basin with sedimentary faults on both sides. At the edge of the basin, alluvial fan deposits dominated by red variegated conglomerates were formed in the lower portion of the Bayingebi Formation. Subsequently, the lake basin expanded and the water flow increased. The climate became warm and humid, forming the upper fan delta to the deep-lake sedimentary facies. In the late Early Cretaceous, influenced by the strike-slip activity of the ATF, large-scale magmatism occurred in Engelwusu and Yingen, and prevalent volcanic activity resulted in a large number of basalts in the Suhongtu Formation in the Bayingebi Basin. The regional multiperiod eruptive rocks are superimposed with sedimentary rocks, and a tectonic inversion occurred in the Late Cretaceous and Paleogene−Quaternary. The basin experienced Triassic-to-Jurassic rifting and the formation of the Lai Basin followed by the comprehensive development stage of the Early Cretaceous Lai Basin, the Late Cretaceous comprehensive sag stage, the Tertiary-to-Quaternary extrusion and uplift, settlement, and local deposition. In short, the distribution pattern of uplift and sag in the basin is strictly controlled by the ATF and its branch faults.

The ATF has undergone multiple periods of activity, including a substantial active period in the late Early Cretaceous, from 100 to 120 Ma.[29] There are many hydrothermal sedimentary rocks distributed along the fault zone (Figure 1b), such as dolomite of the Lower Cretaceous Xiagou Formation in the Jiuxi Basin,[5,8] the Lower Cretaceous Suhongtu Formation and Bayingebi Formation Mudstone in the Hari Sag in the Yinji Basin;[9] analcite dolomitic argillites of the Lower Cretaceous Tengger Formation in the Baiyinchagan Sag;[7] and the Early Cretaceous Bayingebi Formation argillites of the Bayingebi Basin. Across different basins, spanning nearly 1000 km, Early Cretaceous strata exhibit very similar mineral combinations, characterized by dolomite, analcite, and albite. Therefore, it is likely that their genesis is connected via the ATF. Late Cretaceous tectonic activity is the main controlling factor for this type of rock.

4.3. Sedimentary Model of Hydrothermal Rocks.
Based on the analysis of petrology, geochemistry, and tectonic evolution, the deposition of the Bayingebi Formation is controlled by multiphase activity along the ATF. A set of regular hydrothermal sedimentary rocks was formed through the interaction of volcanic eruptions and lake-bottom hydrothermal fluids (Figure 7).

The Early Cretaceous Bayingebi Basin is situated in an extensional tectonic setting. Lake water infiltrated along the fault under the influence of gravity and overburden pressure. During infiltration, the fluid undergoes a long-term water−rock reaction to extract Na^+, Al^{3+}, Si^{4+}, Mg^{2+}, Fe^{2+}, Ca^{2+}, and other ions from the basement rock and contributes hot water to the magma chamber. Then, driven by thermal energy and fluid potential energy, hydrothermal fluid is discharged to the lake basin along the fracture. This continuous circulation of underwater infiltration and convection of hydrothermal fluid provides the lake basin with a heat source and ore-forming ions. When the upwelling hydrothermal fluid moved to the volcanic eruption, the difference in physical and chemical conditions near the vent controlled the precipitation of hydrothermal minerals and formed different mineral assemblages.

Dolomite, ferric dolomite, and analcite precipitated in the spout to form reticular dolomite; when the hydrothermal fluid carried a large amount of Si^{2-}, Al^{3+}, and Na^+ into the lake basin and mixed with the lake water near the spout, speckled analcite dolomite formed. Due to the difference in colloidal and ionic properties, different deposits were formed in areas relatively far from the spout. This allowed the sodium-aluminosilicate hydrothermal fluid to form massive dolomitic analcite.[5] Ca^{2+}, Mg^{2+}, Fe^{2+}, and other ions in hydrothermal fluid are relatively active and can be transported over long distances to areas relatively far from the spout. Owing to mixing with lake water and the addition of lacustrine sediments, striated dolomitic analcite developed in the areas far from the spout. After the hydrothermal fluid was fully mixed with lake water, the low-temperature hydrothermal minerals gradually underwent chemical precipitation and evaporation, forming a gypsum layer in the upper argillites.

4.4. Analysis of Host Rocks as a Repository.
For argillaceous rocks to be a suitable host for an HLW disposal reservoir, it should meet certain geological conditions. The area of the site should not be less than 10 km^2, the continuous distribution of the argillaceous rock geological body should not be less than 100 m, the underground extension width of the clay rock should not be less than 2 km, and the depth of the geological body should be in the range 300−1000 m.[2,30] The dimensions of the upper argillites of the Bayingebi Formation exceed these international selection guidelines. Moreover, the fault activities in the Tamusu area mainly occurred in the Cretaceous and before the Cretaceous, indicating that there has been almost no obvious fault activity since the Quaternary.[20] Certainly, intensive investigations and long-term stability monitoring should be carried out in the Tamusu preselected area. The argillites have a mineral composition that is quite different from that of the French Callovo−Oxfordian clay rock, and the relative percentages of analcite and dolomite are significantly higher than in the Callovo−Oxfordian clay rock. Analcite has a strong "molecular sieve" and ion-exchange functions. Na^+, K^+, and Ca^{2+} in the analcite crystal lattice are not tightly bound to the lattice atom, and cations are easily exchanged with the surrounding environment. Because of its unique geological conditions and mineral composition, the upper portion of the Bayingebi Formation argillites has certain advantages as an HLW repository. The analcite may play a role with respect to radionuclide retention, as discussed in the case of the potential Yucca Mountain host rock[31] and for low- and intermediate-level short-lived radioactive waste in Belgium.[32] In view of functions of analcime channels and molecular sieves, mudstones bearing analcite have advantages over typical clay rocks (host rocks) in terms of radionuclide adsorption, water content, thermal stability, and permeability.[33] The primary pores of mudstone filled with dolomite and analcime cement also highlight the advantages of the uniaxial compressive strength of mudstone, which contribute to engineering construction more than typical clay rocks.[34] In recent studies, it was found that aqueous Se (IV) can be reduced to Se (0)[35] and that aqueous U (VI) could be partially reduced to U (IV) and/or U (V)-containing precipitates (U_3O_8, U_4O_9, etc.) by these Tamusu claystones.[36] Additionally, the advantages and disadvantages of the Bayingebi Formation argillites compared to other potential host rocks remain to be assessed carefully in the future.

5. CONCLUSIONS

The argillites in the upper portion of the Bayingebi Formation exhibit five typical kinds of structures containing higher contents

of dolomite and analcite, which shows enormous potential of the host rock for HLW disposal purpose.

The trace elements in the Bayingebi Formation argillites exhibit a multicomponent combination. The abundance of Mo, Sb, Zn, As, Sr, and Se in the deep-source gas—liquid trace element combination is relatively high; $\Sigma LREE > \Sigma HREE$, indicating a gentle right-angled shape. All argillite samples in the study area are located within the hydrothermal deposition zone on the ternary diagram, indicating the long-term hydrothermal activity of the Yingejing Sag during Early Cretaceous sedimentation.

The tectonic activity of the ATF, from 100 to 120 Ma, is the main controlling factor for the formation of lacustrine hydrothermal sedimentary rocks in the Yingejing Sag in the Bayingebi Basin.

■ AUTHOR INFORMATION

Corresponding Author

Long Xiang − *State Key Laboratory of Nuclear Resources and Environment, East China, University of Technology, Nanchang 330013, China; School of Earth Sciences, East China University of Technology, Nanchang 330013, China;* ◎ orcid.org/0000-0003-1097-598X; Email: xl_son00126@foxmail.com

Authors

Chaocheng Dai − *State Key Laboratory of Nuclear Resources and Environment, East China, University of Technology, Nanchang 330013, China; School of Earth Sciences, East China University of Technology, Nanchang 330013, China*

Yu Zhang − *State Key Laboratory of Nuclear Resources and Environment, East China, University of Technology, Nanchang 330013, China; School of Earth Sciences, East China University of Technology, Nanchang 330013, China*

Xirui Luo − *Jiangxi Bureau of Geology, Nanchang 330036, China*

Xiaodong Liu − *State Key Laboratory of Nuclear Resources and Environment, East China, University of Technology, Nanchang 330013, China*

Shumei Zhang − *Jiangxi Bureau of Geology, Nanchang 330036, China; Non-ferrous Geological Brigade, Jiangxi Bureau of Geology, Ganzhou 341000, China*

Jimei Zheng − *Bureau of Geophysical Prospecting INC., China National Petroleum Corporation, Zhuozhou, Hebei 072750, China*

Complete contact information is available at:
https://pubs.acs.org/10.1021/acsomega.3c09486

Notes

The authors declare no competing financial interest.

■ ACKNOWLEDGMENTS

■ REFERENCES

(1) Andra. Status of the Cigéo Project in France-French industrial geological disposal project. *Presented at: LUCOEX Conference and Workshop, 2−4 June 2015*, Oskarshamn, Sweden, 2015.

(2) Andra. *The Cigeo Project, France's Industrial Centre for Geological Disposal of radioactive waste*. Agence Nationale Pour la Gestion des Dechets Radloactifs, 2020.

(3) Bossart, P.; Bernier, F.; Birkholzer, J.; Bruggeman, C.; Connolly, P.; Dewonck, S.; Fukaya, M.; Herfort, M.; Jensen, M.; Matray, J. M.; Mayor, J. C.; Moeri, A.; Oyama, T.; Schuster, K.; Shigeta, N.; Vietor, T.; Wieczorek, K. Mont Terri rock laboratory, 20 years of research: introduction, site characteristics and overview of experiments. *Swiss Journal of Geosciences* 2017, *110*, 322.

(4) Nagra. *The site for the deep geological repository*. National Cooperative for the Disposal of Radioactive Waste, 2022.

(5) Zheng, R. C.; Wen, H. G.; Li, Y.; Chang, H. L. Compositions and texture of lacustrine exhalative rocks from the Lower Cretaceous Xiagou Formation in Qingxi Sag of Jiuxi Basin, Gansu. *Journal of Palaeogeography* 2018, *20* (1), 1−18.

(6) Li, H.; Liu, Y. Q.; Zhou, X.; Niu, Y. Z.; Li, X.; Liu, Y. J. Origin and geological significance of sedimentary exhalative rocks with "porphyritic" structures in the Middle Permian Pingdiquan Formation, eastern Junggar Basin. *Journal of Palaeogeography* 2017, *19* (2), 211−226.

(7) Zhong, D. K.; Yang, Z.; Sun, H. T.; Zhang, S. Petrological characteristics of hydrothermal sedimentary rocks: A case study of the Lower Cretaceous Tengger Formation in the Baiyinchagan Sag of Erlian Basin, Inner Mongolia. *Journal of Paleogeography* 2018, *20* (1), 20−32.

(8) Wen, H. G.; Zheng, R. C.; Qing, H. R.; Fan, M. T.; Li, Y. N.; Gong, B. S. Primary dolostone related to the Cretaceous lacustrine hydrothermal sedimentation in Qingxi Sag, Jiuquan Basin on the Northern Tibetan Plateau. *Science China: Earth Sciences* 2013, *56* (12), 2080−2093.

(9) Chen, Z. P.; Ren, Z. L.; Yu, C. Y.; Qi, K.; Ren, W. B.; Yang, Y.; Ma, J. Characteristics and genetic analysis of hydrothermal sediment of Lower Cretaceous in Hari Depression, Yin'e Basin. *Earth Science* 2018, *43* (06), 1941−1956.

(10) Zhu, S.; Cui, H.; Jia, Y.; Zhu, X. M.; Tong, H.; Ma, L. C. Occurrence, composition, and origin of analcime in sedimentary rocks of nonmarine petroliferous basins in China. *Marine and Petroleum Geology*. 2019, *104164*.

(11) Rona, P. A.; Hannington, M. D.; Raman, C. V.; Thompson, G.; Tivey, M. K.; Humphris, S. E.; Lalou, C.; Petersen, S. Active and Relict Sea Floor Hydrothermal Mineralization at the TAG Hydrothermal Field, MidAtlantic Ridge. *Economic Geology* 1989, *88*, No. 19892017.

(12) Zhu, S.; Cui, H.; Jia, Y.; Zhu, X. M.; Tong, H.; Ma, L. C. Occurrence, composition, and origin of analcime in sedimentary rocks of non-marine petroliferous basins in China. *Marine and Petroleum Geology* 2019, *133*, No. 104164.

(13) Yang, H.; Li, A.; Cunningham, D.; Yang, X.; Zhan, Y.; Chen, Z. An evolving lithospheric-scale wrench fault system along the eastern end of the Altyn Tagh fault: Kinematics and Quaternary activity of the Heishan fault system, western China. *Tectonics* 2023, *42*, No. e2023TC007764.

(14) Li, H.; Chevalier, M. L.; Tapponnier, P.; Pan, J.; Van der Woerd, J.; Mériaux, A. S. Block tectonics across Western Tibet and multi-millennial recurrence of Great Earthquakes on the Karakax fault. *Journal of Geophysical Research: Solid Earth* 2021, *126* (12), No. e2021JB022033.

(15) Molnar, P.; Tapponnier, P. Cenozoic tectonics of Asia: Effects of a continental collision: Features of recent continental tectonics in Asia can be interpreted as results of the India-Eurasia collision. *Science* 1975, *189* (4201), 419−426.

(16) Tapponnier, P. E.; Peltzer, G.; Dain, A.; Armijo, R.; Cobbold, P. R. Propagating extrusion tectonics in Asia: New insights from simple experiments with plasticine. *Geology* 1982, *10*, 611−616.

(17) Tapponnier, P. Oblique Stepwise Rise and Growth of the Tibet Plateau. *Science* 2001, *294* (5547), 1671−1677.

(18) Zhang, C. Y.; Nie, F. J.; Jiao, Y. Q.; Deng, W.; Peng, Y. B.; Hou, S. R.; Dai, M. J.; Ye, T. F. Characterization of ore forming fluids in the Tamusu sandstone type uranium deposit, Bayingobi Basin, China: constraints from trace elements, fluid inclusions and C−O−S isotopes. *Ore Geology Reviews*. 2019, *102999*.

(19) Xiang, L.; Liu, X. D.; Liu, P. H.; Dai, C. C.; Jiang, M. X. Genesis of host rock in the Tamusu Mudstone pre-selected area in Northwest China for high-level radioactive waste geological disposal purposes. *Swiss Journal of Geosciences* **2023**, *116*, 6.

(20) Rao, Z.; Li, G. R.; Liu, X. D.; Liu, P. H.; Li, H. H.; Liu, S.; Zhu, M. Q.; Guo, C.; Ni, F. J.; Gong, Z. J. Fault activity in clay rock site candidate of high level radioactive waste repository, Tamusu Inner Mongolia. *Minerals* **2021**, *11* (9), 941.

(21) Li, T. The statistical characteristics of the abundance of chemical elements in the Earth's Crust. *Geology and Exploration* **1992**, *28*, 17.

(22) Davies, G. R.; Smith, L. B., Jr Structurally controlled hydrothermal dolomite reservoir facies: An overview. *AAPG Bulletin* **2006**, *90*, No. 16411690.

(23) Stoffers, P. Active Pitcairn Hotspot Found. *Marine Geology* **1990**, *95*, 5155.

(24) Zhu, D. Y.; Jin, Z. J.; Hu, W. X. Hydrothermal recrystallization of the Lower Ordovician dolomite and its significance to reservoir in northern Tarim Basin. *Science China: Earth Sciences* **2010**, *53*, No. 368381.

(25) Taylor, S. R.; Mclennan, S. M. The Continental Crust: its Composition and Evolution. *Physics of the Earth and Planetary Interiors* **1986**, *42*, No. 196197.

(26) Crerar, D. A.; Namson, J.; Chyi, M. S.; Williams, L.; Feigenson, M. D. Manganiferous Cherts of the Franciscan Assemblage; I, General Geology, Ancient and Modern Analogues, and Implications for Hydrothermal Convection at Oceanic Spreading Centers. *Economic Geology* **1982**, *77*, No. 519540.

(27) Choi, J. H.; Hariya, Y. Geochemistry and Depositional Environment of MnOxide Deposits in the Tokoro Belt, Northeastern Hokkaido, Japan. *Economic Geology* **1992**, *87* (5), No. 12651274.

(28) Zhang, C. Y.; Nie, F. J.; Hou, S. R.; Wang, J. L.; Deng, W.; Zhang, L. Tectonic Evolution Characteristics of Bayingebi Basin and Its Control on the Mineralization of Sandstone Type Uranium Deposits. *Uranium Geology* **2015**, *31*, No. 384388.

(29) Li, H. B.; Yang, J. S.; Xu, Z. Q.; Sun, Z. M.; Tapponnier, P.; Woerd, J.; Meriaux, A. S. The constraint of the Altyn Tagh fault system to the growth and rise of the northern Tibetan plateau. *Earth Science Frontiers* **2006**, *13*, 5979.

(30) Kasbohm, J.; Pusch, R.; Lan, N. T.; Thao, H. M. Labscale performance of selected expandable clays under HLW repository conditions. *Environmental Earth Sciences* **2013**, *69*, No. 25692579.

(31) Bish, D. L. Natural Zeolites and Nuclear-Waste Management: The Case of Yucca Mountain, Nevada, USA. In: *Natural Microporous Materials in Environmental Technology*. NATO Science Series, vol *362*. Springer: Dordrecht. 1999; pp 177−191.

(32) Misaelides, P. Clay minerals and zeolites for radioactive waste immobilization and containment. In: *Modified Clay and Zeolite Nanocomposite Materials*. Elsevier: Amsterdam. 2019; pp 243−274.

(33) Yu, H. D.; Lu, C.; Chen, W. Z.; Li, H. Permeability changes in fractured Tamusu mudstone in the context of radioactive waste disposal. *Bulletin of Engineering Geology and the Environment* **2021**, *80* (10), 7945−7957.

(34) Wang, Y.; Liang, H. A.; Hu, Q. B.; Chen, H. K.; Wang, C.; Xie, Z. Study on orrelation between mineral composition and elastic modulus of clay ock in Tamusu. *Chongqing Architecture* **2018**, *17*, 18−21.

(35) Wu, J.; Guo, B.; Kang, M.; Kang, Y.; Jin, W.; Wu, H.; Wu, S. Comparative study on the reductive immobilization of Se (IV) by Beishan granite and Tamusu claystone. *Appl. Geochem.* **2022**, *146*, No. 105447.

(36) Kang, M.; Kang, Y.; Wu, H. Y.; Qin, D.; Dai, Z.; Wang, J. The redox reactions of U (VI)/UO2 on Tamusu claystone: Effects of Fe2+/Fe3+ and organic matters. *Chemosphere* **2024**, *348*, No. 140754.